Supporting Information of

Facile and Versatile Construction of MOF@COF Heterostructures in Atmospheric Air for Enhanced CO_2 Photoreduction

*Ming-Li Ma[1,†], Le-Chen Zheng[1,†], Rui Li[*1], and Yabo Xie[1]*

1. Beijing Key Laboratory for Green Catalysis and Separation and Department of Chemical Engineering, College of Materials Science and Engineering, Beijing University of Technology, Beijing, P. R. China 100124.

* Corresponding author:

E-mail address: lirui1@bjut.edu.cn (R. Li).

† Both authors contributed equally to this work.

Calculations

Diffuse absorption spectra were calculated into Tauc plots using the equations below:

$$(\alpha h\upsilon)^{1/r} = C\left(h\upsilon - E_g\right), \qquad (Eq\ S1)$$

where E_g is the optical bandgap, $h\upsilon$ is the energy of the incident photon, C is a constant and α is the diffuse absorption coefficient. The exponent r denotes the nature of the transition. A value of $r = 1/2$ is used here as the common practice in MOF/COF analysis [1].

For a thin film with neglected scattering and reflectance, the absorption coefficient could be roughly estimated using a simple linear equation:

$$\alpha = 2.303\ A\ /\ t, \qquad (Eq\ S2)$$

where t is the thickness of the thin film, and A is the measured absorbance [2].

Tables

Table S1. Surface areas and CO_2 uptakes of samples examined at 273 K.

Samples	BET surface area (m^2/g)	Total pore volume (cm^3/g)	CO_2 uptake at 1 bar (cm^3/g)
NUiO	975.5	0.4633	30.42
TpPa	822.4	0.5946	56.32
NUT-D-3M	651.9	0.3907	43.90
NUT-D-4M	547.2	0.4080	42.28

Table S2. CO_2RR performances of representative MOF/COF-based hybrid photocatalysts.

Photocatalysts	Light sources	Reaction media	Products	Production rates ($\mu mol \cdot g^{-1} \cdot h^{-1}$)	Ref.
NUT-D-3M	300W Xe lamp	H_2O TEA	CO	50.88	**This work**
NUT-D-4M	300W Xe lamp	H_2O TEA	CO	57.88	**This work**
TpPa-1/ZIF-8	40W LED	H_2O	CO	43.94	[3]
NH_2-MIL-125@COF-OH-3	300W Xe lamp	H_2O	CO	22.93	[4]
NH_2-MIL-68(In)@TP-TA	300W Xe lamp	H_2O	CO CH_4	25.00 11.67	[5]
C60@TpPa	LED	H_2O	CO	48.16	[6]
TTCOF/ NH_2-UiO-66	300W Xe lamp	H_2O	CO	6.56	[7]
NH_2-UiO-66/$CdIn_2S_4$	Visible light	H_2O	CO CH_4	11.24 2.92	[8]

Figures

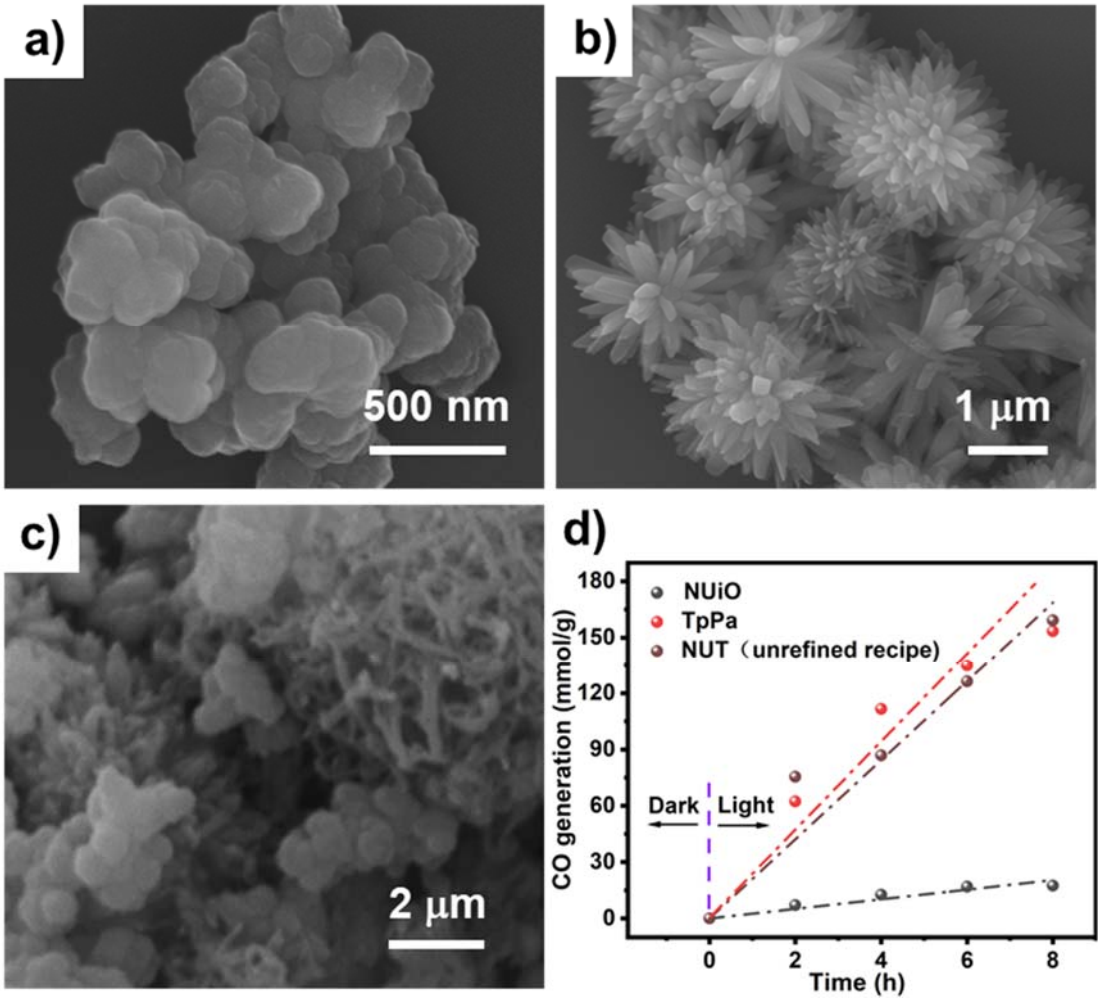

Figure S1. NUT synthesized in air using unrefined recipe. Electron micrographs of (a) NUiO and (b) TpPa illustrating spheroidal and dendritic aggregates, respectively. (c) Electron micrographs of NUT obtained in common air using the original synthesis recipe, exhibiting the lack of interphase interactions between the MOF and COF crystals. (d) The CO yield of this weakly contacted NUT is inferior to that of the individual TpPa.

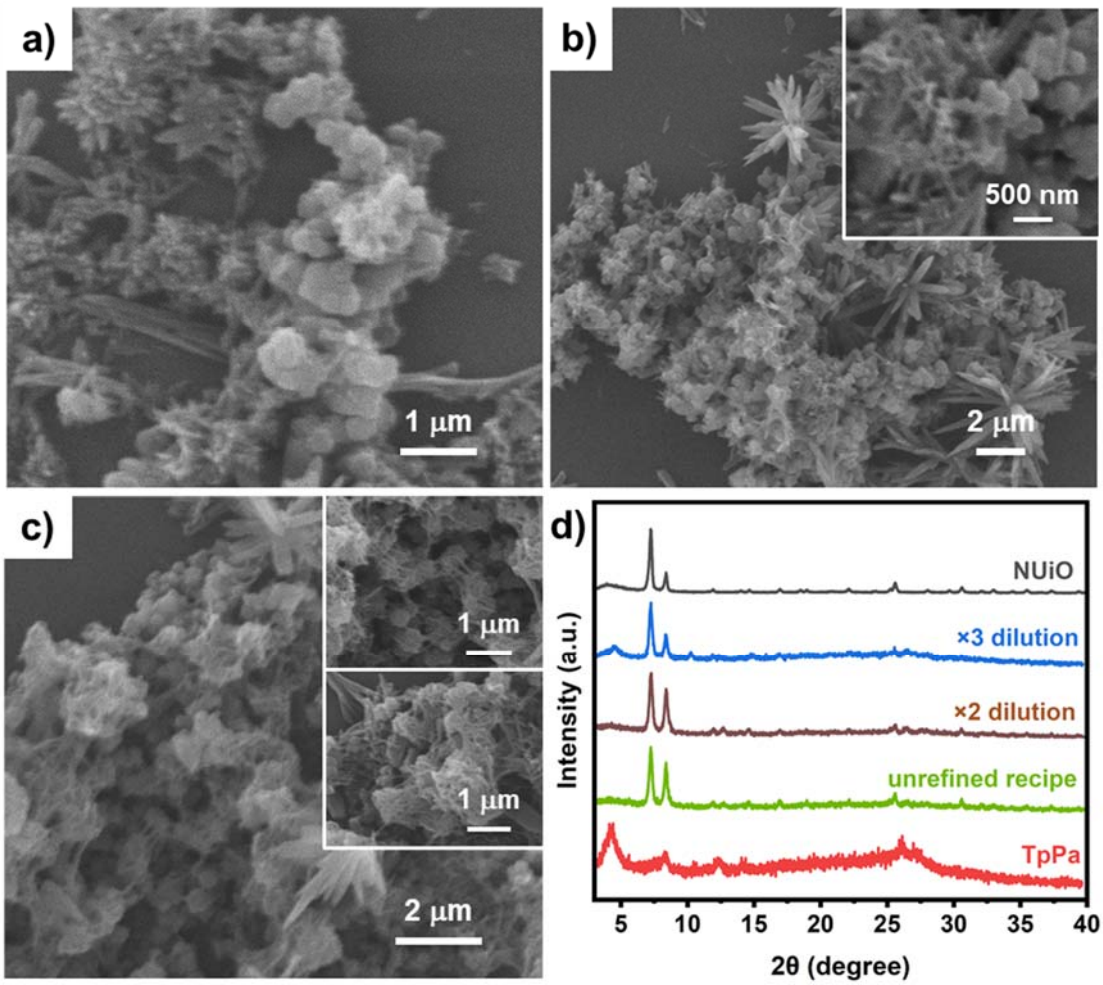

Figure S2. NUT synthesized in air with reduced supersaturation. (a-c) Electron micrographs of NUT samples synthesized with diluted recipes: (a) unrefined recipe, (b) solvent amount doubled, and (c) solvent amount tripled. The MOF-COF connections were unambiguously enhanced when the supersaturation of the synthesis mixtures was gradually reduced. Insets of panels (b) and (c) display the attachment of TpPa on NUiO surfaces. Note that with diluted solutions, the width of TpPa rods was decreased. (d) Sample XRD patterns reveal promoted TpPa contents with the increase of dilution, potentially attributing to the reduced energy barrier of crystallization when heterogeneous nucleation on MOF surfaces predominates.

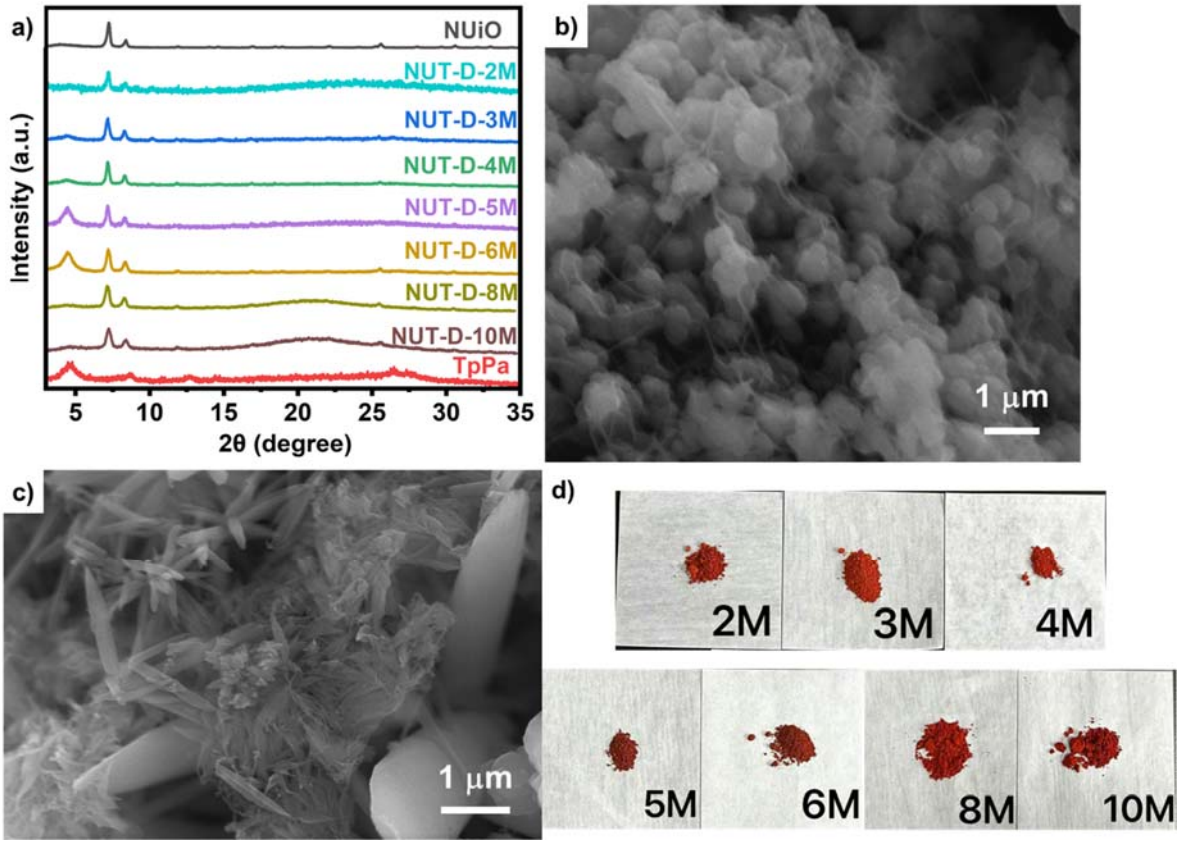

Figure S3. NUT synthesized in air with altered acidity. (a) XRD patterns of NUT-D samples synthesized using varied concentrations of acetic acid ranging from 2 to 10 M. The characteristic peaks of TpPa increased at moderate acidity of 2~4 M. A radical increase of the peak below 5° at the expense of other TpPa peaks was observed at high acid contents of 5~6 M, suggesting the damaged crystal structure of the COF. Further increasing the acid concentration beyond 8 M led to the complete disappearance of TpPa peaks, accompanied by the emergence of amorphous materials. (b) Electron micrograph of NUT-D-4M exhibiting enhanced MOF-COF contact. Note that the TpPa anchored on NUiO possessed a fibrous morphology. In fact, vastly different morphologies from thick rods to thread-like fibers were detected for TpPa when 4 M acetic acid was employed, as shown in (c), which might imply the onset of COF impairment. (d) Photograph of NUT-D samples with different acid concentrations. The samples synthesized with different acetic acid demonstrated altered shades of red, indicating their changed physicochemical properties.

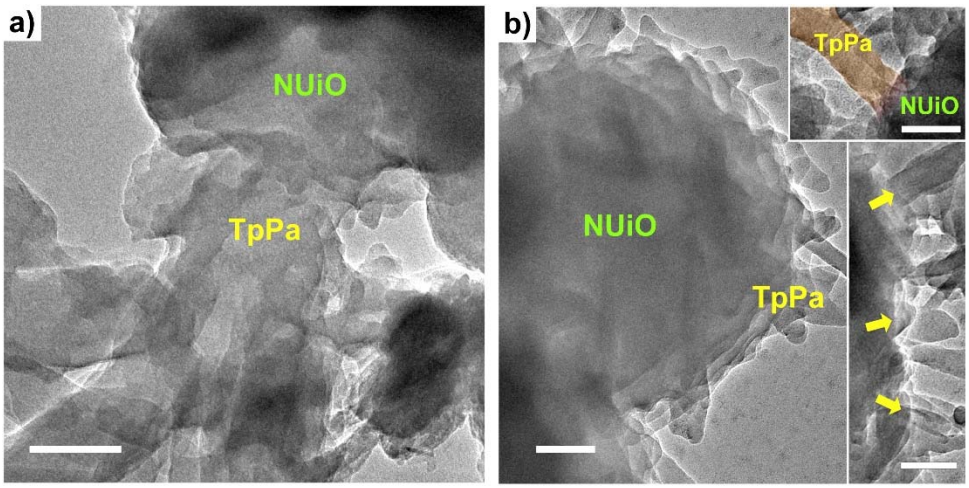

Figure S4. High resolution images illustrating the fusion between MOF and COF. TEM images of the MOF-COF intersections of (a) NUT-D-3M and (b) NUT-D-4M. Intensive feeding of TpPa rods into NUiO spheres were observed in both samples, resulting in roughened crystal surfaces. Additional examples of the seamless fusions were demonstrated in the insets of panel b, where a TpPa rod (up) and intersecting points (down) were highlighted using altered color and yellow arrows, respectively.

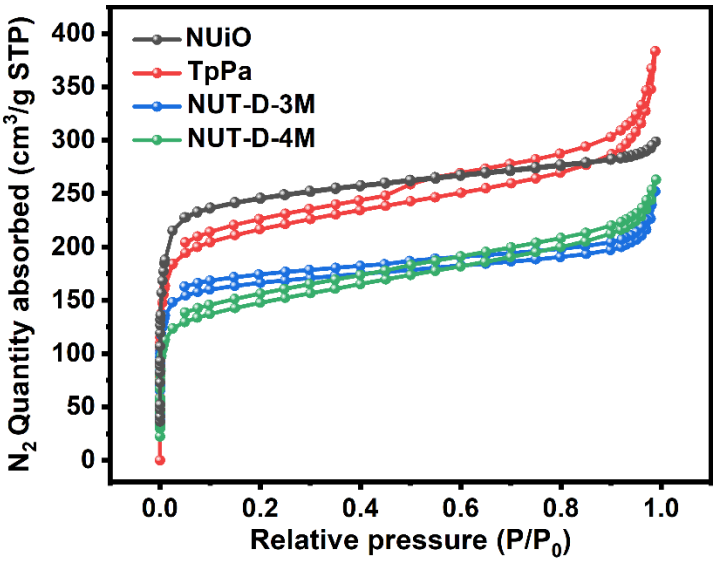

Figure S5. N_2 adsorption isotherms of samples measured at 77K.

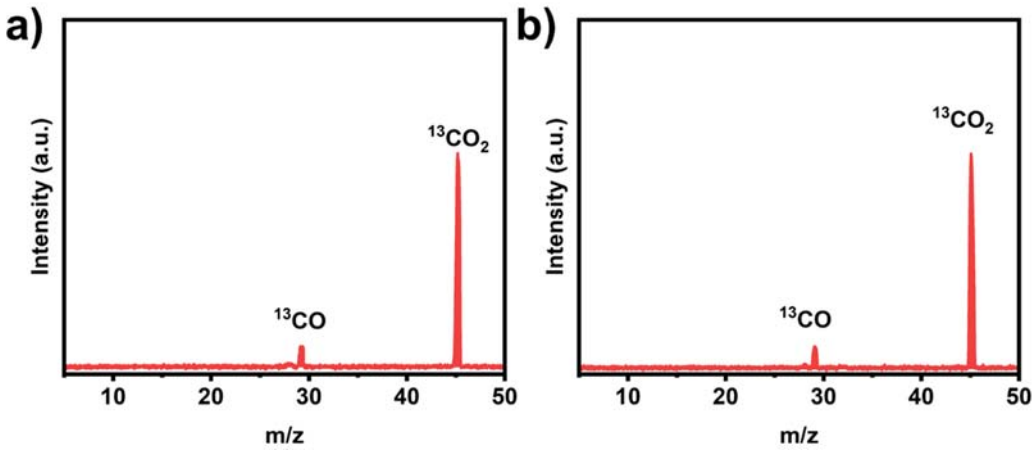

Figure S6. Mass spectra of the products originated from isotope-labelled $^{13}CO_2$. The effluent gases of (a) NUT-D-3M and (b) NUT-D-4M were analyzed using mass spectroscopy. For both systems, ^{13}CO was identified as the sole product, with the presence of unreacted $^{13}CO_2$ concurrently witnessed. The CO_2 converting capacity and high selectivity of the composite catalysts were hence unambiguously verified.

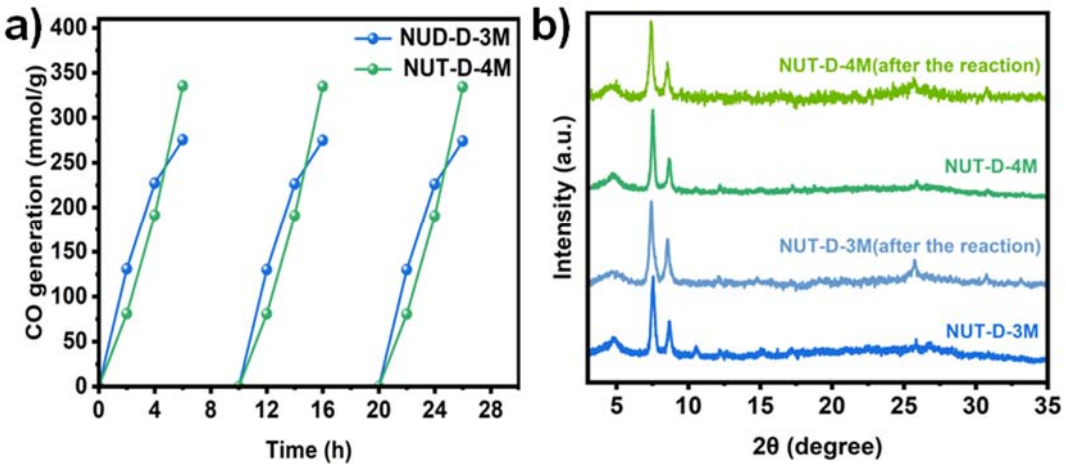

Figure S7. Stability of the MOF@COF composites. The stability of NUT-D-3M and 4M catalysts was evaluated in repeated reaction cycles. Almost identical activities were observed for both samples in three reaction cycles (a). Only subtle differences were detected in the XRD patterns after the reaction (b), suggesting that the crystal structures of the materials were essentially preserved. The observations illustrated the robust stability of the MOF@COF composites.

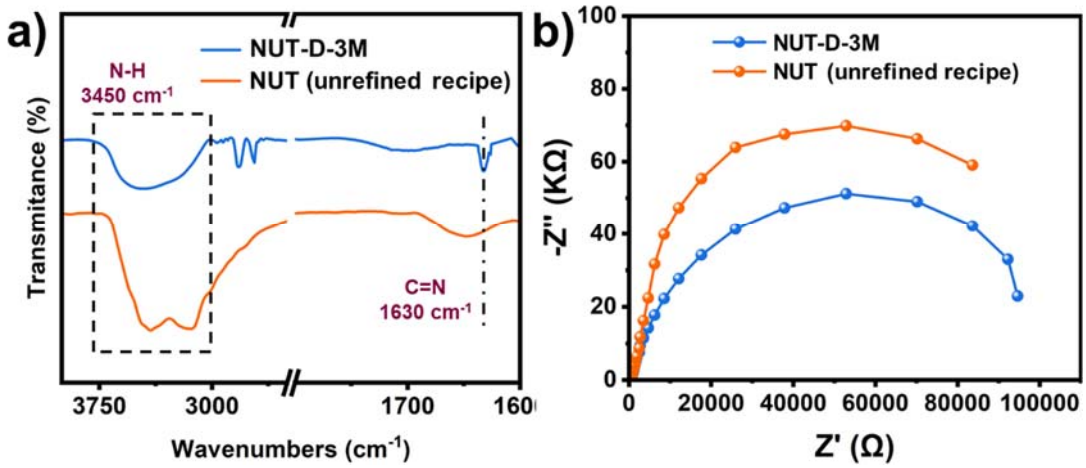

Figure S8. Assessment of bonding status and electron transfer efficiency in NUT samples. The FTIR (a) and EIS (b) spectra of the NUT synthesized using the unrefined recipe were measured. Compared with the FTIR spectrum of NUT-D-3M, apparently higher N-H but lower C=N peaks were manifested for the unrefined NUT, indicating its deficient interphase contact. A drastically increased electrochemical impedance was concurrently perceived for this sample, alluding the significant influence of interphase interactions on electron transfer efficiency. With the transfer of charges inhibited, a poor CO_2RR performance is anticipated for the weakly contacted NUT.

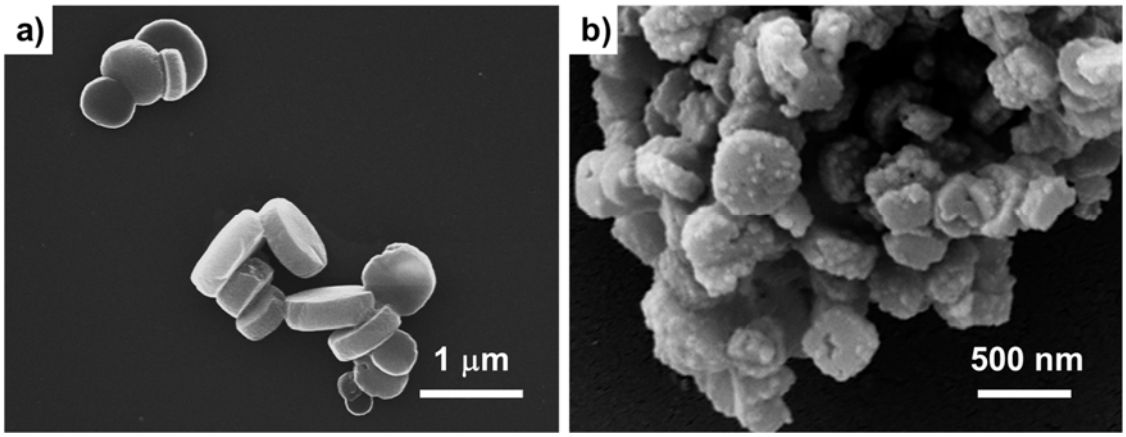

Figure S9. NML synthesized in air using unrefined recipe. Electron micrographs of (a) NMiL and (b) NML samples. The cylindrical morphology of NMiL was maintained after hybridization. Spheroidal LZU dots were scarcely deposited onto MOF surfaces, indicating weak interphase contact.

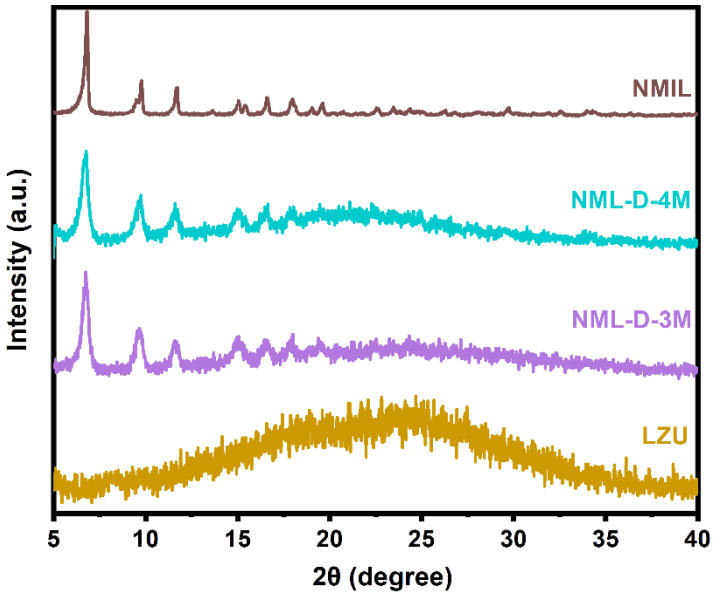

Figure S10. XRD patterns of refined NML samples. XRD patterns of NML-D-3M and 4M, which match well with the patterns of NMiL and LZU, validating the presence of both phases in the composite. The LZU content appears to increase with the concentration of the acid modulator, consistent with the trend observed for NUT samples.

References

[1] F.-M. Zhang, J.-L. Sheng, Z.-D. Yang, X.-J. Sun, H.-L. Tang, M. Lu, H. Dong, F.-C. Shen, J. Liu, Y.-Q. Lan, Rational design of MOF/COF hybrid materials for photocatalytic H_2 evolution in the presence of sacrificial electron donors, Angew. Chem. Int. Edit., 57 (2018) 12106-12110. https://doi.org/10.1002/anie.201806862

[2] A. Javed, N. Khan, S. Bashir, M. Ahmad, M. Bashir, Thickness dependent structural, electrical and optical properties of cubic SnS thin films, Mater. Chem. Phys., 246 (2020) 122831. https://doi.org/10.1016/j.matchemphys.2020.122831

[3] R.-G. Yang, Y.-M. Fu, H.-N. Wang, D.-P. Zhang, Z. Zhou, Y.-Z. Cheng, X. Meng, Y.-O. He, Z.-M. Su, ZIF-8/covalent organic framework for enhanced CO_2

photocatalytic reduction in gas-solid system, Chem. Eng. J., 450 (2022) 138040. https://doi.org/https://doi.org/10.1016/j.cej.2022.138040

[4] J. Wang, L. Wang, D. Zhang, Y. Wang, J. Li, F. Zhou, J. Huang, Y.N. Liu, Covalently connected core-shell NH_2-MiL-125@COFs-OH hybrid materials for visible-light-driven CO_2 reduction, J. Colloid Interface Sci., 637 (2023) 1-9. https://doi.org/10.1016/j.jcis.2022.12.154

[5] L. Wang, J. Mao, G. Huang, Y. Zhang, J. Huang, H. She, C. Liu, H. Liu, Q. Wang, Configuration of hetero-framework via integrating mof and triazine-containing COF for charge-transfer promotion in photocatalytic CO_2 reduction, Chem. Eng. J., 446 (2022) 137011. https://doi.org/https://doi.org/10.1016/j.cej.2022.137011

[6] Y.-O. He, Y.-M. Fu, X. Meng, L. Xue, R.-G. Yang, J.-X. Qu, Z.-M. Su, H.-N. Wang, Enhanced visible light-driven CO_2 reduction activity induced by Z-scheme heterojunction photocatalyst C_{60}/TpPa (COF), Appl. Catal. A-Gen., 663 (2023) 119320. https://doi.org/10.1016/j.apcata.2023.119320

[7] Q. Niu, S. Dong, J. Tian, G. Huang, J. Bi, L. Wu, Rational design of novel cof/mof s-scheme heterojunction photocatalyst for boosting CO_2 reduction at gas–solid interface, ACS Appl. Mater. Interfaces, 14 (2022) 24299-24308. https://doi.org/10.1021/acsami.2c02439

[8] L.-f. Hong, R.-t. Guo, Z.-w. Zhang, Y. Yuan, X.-y. Ji, Z.-d. Lin, W.-g. Pan, Fabrication of porous octahedron-flowerlike microsphere NH_2-UiO-66/$CdIn_2S_4$ heterojunction photocatalyst for enhanced photocatalytic CO_2 reduction, J. CO_2 Util., 51 (2021) 101650. https://doi.org/10.1016/j.jcou.2021.101650